

# Magnetic Soft Millirobots 3D Printed by Circulating Vat Photopolymerization to Manipulate Droplets Containing Hazardous Agents for In Vitro Diagnostics

Aiwu Zhou, Changyu Xu, Pojchanun Kanitthamniyom, Chelsea Shan Xian Ng, Gerard Joseph Lim, Wen Siang Lew, Shawn Vasoo, Xiaosheng Zhang, Guo Zhan Lum, and Yi Zhang\*

3D printing via vat photopolymerization (VP) is a highly promising approach for fabricating magnetic soft millirobots (MSMRs) with accurate miniature 3D structures; however, magnetic filler materials added to resin either strongly interfere with the photon energy source or sediment too fast, resulting in the nonuniformity of the filler distribution or failed prints, which limits the application of VP. To this end, a circulating vat photopolymerization (CVP) platform that can print MSMRs with high uniformity, high particle loading, and strong magnetic response is presented. After extensive characterization of materials and 3D printed parts, it is found that  $\text{SrFe}_{12}\text{O}_{19}$  is an ideal magnetic filler for CVP and can be printed with 30% particle loading and high uniformity. By using CVP, various tethered and untethered MSMRs are 3D printed monolithically and demonstrate the capability of reversible 3D-to-3D transformation and liquid droplet manipulation in 3D, an important task for in vitro diagnostics that are not shown with conventional MSMRs. A fully automated liquid droplet handling platform that manipulates droplets with MSMR is presented for detecting carbapenem antibiotic resistance in hazardous biosamples as a proof of concept, and the results agree with the benchmark.

## 1. Introduction

Soft millirobots that are on the millimeter or smaller scale, can actively deform and morph their shapes to achieve dexterous locomotion in addition to a diverse range of mechanical functionalities.<sup>[1–6]</sup> These miniature robots have one unique advantage in that they can exploit their small size to operate in highly confined environments; therefore, it is expected that these

robots will transform a vast range of biomedical applications.<sup>[7–11]</sup> Magnetic actuation is one of the most popular method among the available actuation methods to control soft millirobots,<sup>[12,13]</sup> because of its remote and wireless control, ability to induce rapid response, and ease of implementation.<sup>[13,14]</sup> The rapid response helps realize a short latency between the stimulation and shape morphing, and it allows millirobots to work in harsh environments with abrupt changes and unknown variations.<sup>[15]</sup>

Magnetic soft millirobots (MSMRs) can be fabricated by shaping magnetically responsive elastomers using molding, 2D lithography techniques<sup>[14,16,17]</sup> and 3D printing.<sup>[18–23]</sup> Among these fabrication methods, 3D-printing is promising because it can potentially fabricate MSMR monolithically beyond 2D configurations.<sup>[4,6,19–24]</sup> Several MSMRs can morph into 3D structures upon actuation have already been fabricated using

extrusion-based 3D printing, but these MSMRs are all fabricated with a 2.5D initial geometry. Although such extrusion-based 3D printing methods show great promise, their print quality is known to be strongly influenced by the nozzle movement and extrusion rate.<sup>[25]</sup> In addition to extrusion-based 3D printing, vat photopolymerization (VP) is another popular 3D printing method used to fabricate magnetic millirobots. The VP method generates 3D structures by curing resins in a vat

A. Zhou  
Singapore Centre for 3D Printing  
School of Mechanical and Aerospace Engineering  
Nanyang Technological University  
50 Nanyang Avenue, Singapore 639798, Singapore  
C. Xu, P. Kanitthamniyom, C. S. X. Ng, G. Z. Lum  
School of Mechanical and Aerospace Engineering  
Nanyang Technological University  
50 Nanyang Avenue, Singapore 639798, Singapore

 The ORCID identification number(s) for the author(s) of this article can be found under <https://doi.org/10.1002/adma.202200061>.

DOI: 10.1002/adma.202200061

G. J. Lim, W. S. Lew  
School of Physical and Mathematical Sciences  
Nanyang Technological University  
50 Nanyang Avenue, Singapore 639798, Singapore  
S. Vasoo  
National Center for Infectious Disease  
Tan Tock Seng Hospital  
11 Jln Tan Tock Seng, Singapore 308433, Singapore  
X. Zhang, Y. Zhang  
School of Electronic Science and Engineering  
University of Electronic Science and Technology of China  
2006 Xiyuan Avenue, Chengdu, Sichuan 611731, China  
E-mail: yi\_zhang@uestc.edu.cn

layer-by-layer with an ultraviolet (UV) photon energy source. A critical advantage of VP-based 3D printing is that it offers high-quality prints on a small scale. Indeed, two-photon polymerization, which is a VP-based 3D printing method, has been used to fabricate microscale magnetic robots with complex 3D geometries.<sup>[26–29]</sup> However, these magnetic robots have rigid bodies and low magnetic-particle-loading ratios; therefore, they cannot actively morph their shapes to achieve sophisticated mechanical functionalities. The feasibility of using VP-based 3D printing methods to create MSMRs with uniform and high magnetic-particle loading in addition to realizing true 3D initial geometries and 3D shaping morphing capabilities is yet to be investigated.

If VP-based 3D printing methods can indeed create highly functional MSMRs, these robots will be highly beneficial for droplet manipulation. Many MSMRs have shown the capability of manipulating solid objects with high degree of freedom and dexterity,<sup>[30]</sup> but seldomly are they used to manipulate liquid or other soft matters. Liquid manipulation is crucial for a variety of biomedical applications, especially in vitro diagnostics. Magnetic platforms, such as magnetic digital microfluidics, use magnetic force to manipulate liquid droplets on an open surface for in vitro diagnostics.<sup>[31]</sup> Droplets on the magnetic digital microfluidic platform function as biochemical reaction chambers. Traditionally, these droplets are manipulated by magnetic

particles or a soft magnetic substrate.<sup>[31]</sup> Although several tools have been developed to facilitate droplet manipulation, droplet motion remains restricted to a 2D plane. However, complex in vitro diagnostic assays require the transfer of droplets across different platforms with 3D motion. To the best of our knowledge, no MSMR has been demonstrated for droplet manipulation, and conventional automatic liquid handling systems are not designed for droplet manipulation on an open surface. Hence, it is highly desirable to fabricate functional MSMRs that can effectively manipulate the droplets in 3D to address current limitations in automated liquid manipulation for droplet-based in vitro diagnostic platform.

Here we report a VP technology that can 3D print MSMRs with a composite resin with a high loading of magnetic particles. We have selected relatively large micrometer-sized  $\text{SrFe}_{12}\text{O}_{19}$  particles as fillers to enhance the magnetic response of our MSMR and reduce the interference with the photon energy source. However, large particles tend to form sediments rapidly in the liquid resin, which causes an inhomogeneous distribution of magnetic particles in the final print (Figure 1). Therefore, we developed a circulating VP (CVP) technology by integrating a circulation system with VP platforms to homogenize the composite resin during printing so that homogeneous particle distribution can be achieved with up to 30% micro- $\text{SrFe}_{12}\text{O}_{19}$  magnetic-particle fillers (Figure 1a). We can

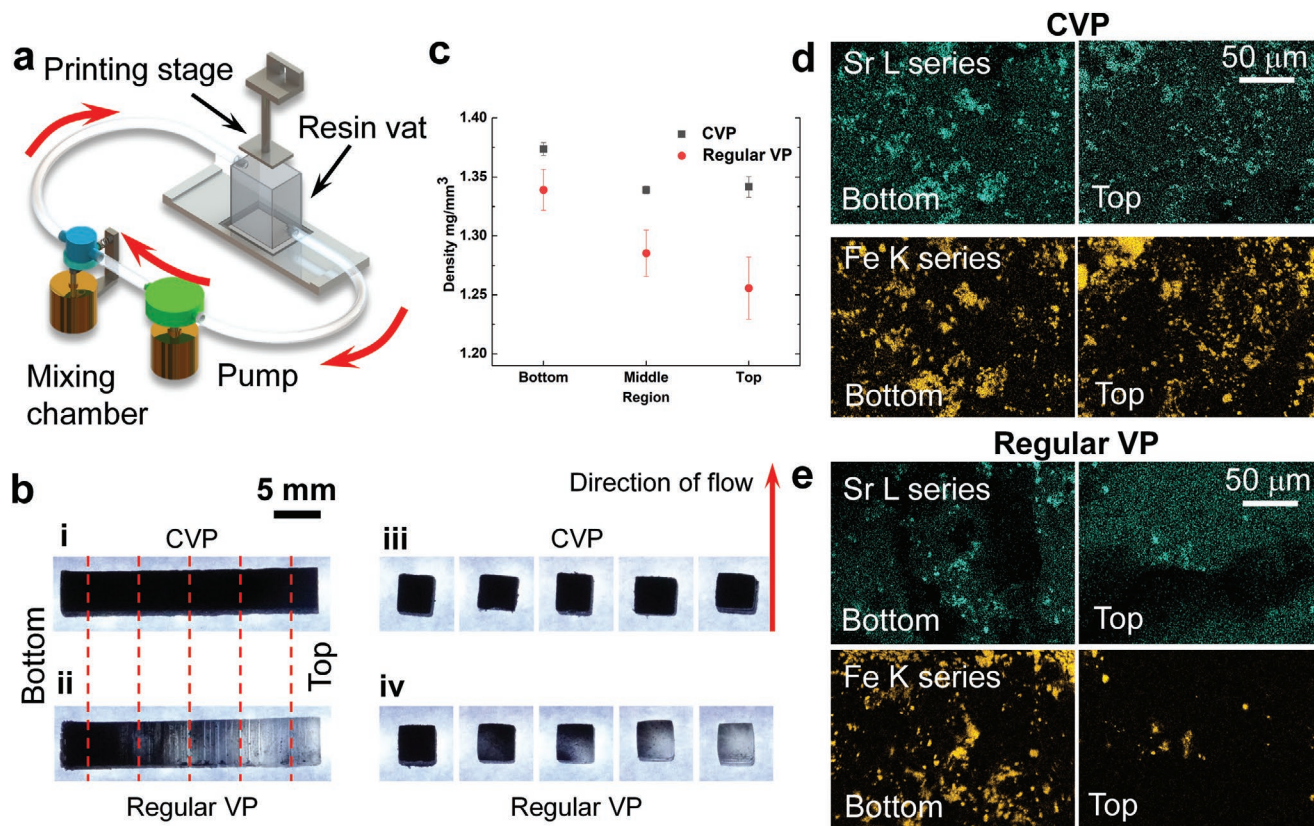


**Figure 1.** Circulating vat photopolymerization (CVP). a) Schematic of CVP system. b) Comparison of specimens printed using CVP and regular. “Bottom” is the portion that is printed first, and “Top” is the portion that is printed last. Parts (iii) and (iv) show the cross-section views of the specimens in (i) and (ii) at the location indicated by the red dash line. c) The density of the top, middle and bottom segments of the specimens shown in (b). d,e) EDX element mapping of Sr and Fe in specimens shown in (b), respectively.

print MSMRs with true initial 3D geometries and demonstrate rapid 3D-to-3D transformation upon magnetic actuation. Another objective of this study is to create MSMRs that can effectively manipulate liquid droplets and establish a MSMR-empowered automated droplet microfluidic handling platform that remotely manipulates hazardous biological agents in droplets across different platforms in 3D for in vitro diagnostics of antibiotic-resistant bacteria.

In this reported, we first explain how CVP operates and present how the SrFe<sub>12</sub>O<sub>19</sub>-based magnetic composite resin is optimized based on extensive characterizations of the raw materials and the 3D printed parts. Next, the magnetically driven locomotion and droplet manipulation of several MSMRs 3D printed by CVP are demonstrated. In the end, the operation and results obtained by the MSMR-empowered in vitro diagnostic platform are presented.

## 2. Development of CVP

One of the biggest challenges for printing composite resin using VP is the rapid sedimentation of particle fillers that causes inhomogeneous particle distribution in the printed parts or even failed prints (Figure 1b).<sup>[32]</sup> Although the sedimentation of nanoparticles is slow, their strong interference with the photon energy source is a major hurdle to realizing high-particle-loading ratios. Several magnetic millirobots printed via two-photon polymerization contain only <1% (w/v) magnetic particles.<sup>[26,27,33]</sup> Therefore, it is challenging to induce a strong magnetic response and large deformation for these soft robots when dealing a magnetization profile with such a low particle loading. Although large micrometer-sized particles can partially mitigate the light interference and hence achieve a high particle-loading ratio, these large particles sediment rapidly, which can result in an inhomogeneous distribution of magnetic materials in the final print. The sediments may completely block the light path and stop the printing process.

To overcome this issue, the proposed CVP method employs a circulation system that homogenizes the composite resin during printing (Figure 1a). The composite resin is withdrawn from a customized mini resin vat via an outlet close to the bottom and pumped into a mixing chamber for homogenization before being injected back into the resin vat via an inlet on the other side. Alternatively, two bifurcating fluidic manifolds are fixed to the original resin vat for large builds (Figure S1.1, Supporting Information). Two specimens (5 × 5 × 30 mm<sup>3</sup>) are printed with a composite resin that comprises a polyurethane (PU)-like resin and SrFe<sub>12</sub>O<sub>19</sub> particles as the magnetic filler; the specimen printed by CVP (Figure 1bi) shows a uniform distribution of magnetic particles. In contrast, the specimen printed by regular VP (Figure 1bii) shows a gradual decrease in the particle content from the bottom (first printed) to the top (last printed) because of particle sedimentation during printing. The cross-section views of the CVP specimens show uniform particle distribution in various planes (Figure 1biii), and no concentration gradient of magnetic particles along the direction of flow is not observed. In contrast, the specimen printed by regular VP shows nonuniform particle distribution in the cross-section view; its top portion becomes almost transparent

because of particle sedimentation (Figure 1biv). A total of 3 2 mm thick segments were sliced from the top, middle and bottom region of each specimen, and their density was measured using Archimedes' method (Figure 1c).<sup>[34]</sup> The three segments from the specimen printed by CVP demonstrated a similar density. In contrast, the three segments from the specimen printed by regular VP demonstrated distinct densities, with the highest at the bottom and the lowest at the top. This is because magnetic particles sediment as the printing proceeded, which causes the effective particle-loading ratio in the resin to decrease, thereby causing a lower density in the portion that was printed last. The uniformity of the magnetic particles in the two specimens was further confirmed by energy dispersive X-ray analysis (EDX) element mapping. The specimen printed by CVP showed a more uniform Sr and Fe distribution in both the top and bottom portions of the specimen (Figure 1d). In contrast, the particle distribution in the specimen printed by regular VP was nonuniform, as indicated by large regions devoid of Sr and Fe elements at the top (Figure 1e).

The absorbance and sedimentation rate of the magnetic fillers in the composite resin were critical for CVP. Three types of magnetic particle fillers of similar size—SrFe<sub>12</sub>O<sub>19</sub> (3–6 μm), Fe<sub>3</sub>O<sub>4</sub> (2–4 μm), and NdFeB (nominal size of 5 μm)—were examined by UV-vis spectrometry at the same concentration. In comparison, SrFe<sub>12</sub>O<sub>19</sub> showed a significantly lower absorbance at 405 nm compared to the other two types of magnetic particles (Figure 2a), which allows higher particle-loading ratios in the composite. The absorbance was particularly high for Fe<sub>3</sub>O<sub>4</sub>, which saturated the spectrometer at 0.2% w/w. The absorbance decreased with increasing particle size (Figure 2b), as expected, according to Mie theory.<sup>[35]</sup> The coarse SrFe<sub>12</sub>O<sub>19</sub> particle (6–12 μm) showed the lowest absorbance, and the fine particle (2.4–3 μm) showed the highest absorbance among the three types of SrFe<sub>12</sub>O<sub>19</sub> particles. The sedimentation rate was measured by a modified Westergren method. The normalized sedimentation (Figure 2c) confirmed that large particles sediment at a more rapid rate. Although the coarse SrFe<sub>12</sub>O<sub>19</sub> particles have lower absorbance than the medium ones, the large particles accumulate in the circulation system. Based on these observations, we selected medium SrFe<sub>12</sub>O<sub>19</sub> particles for our subsequent studies.

In the CVP, the circulation system can operate continuously throughout the entire printing process, or in a periodic mode wherein the pump is switched on between the photocuring steps. The continuous mode is relatively easy to implement but the shear stress generated during the photocuring step may cause the partially crosslinked layer to fall off the printing stage. The periodic mode does not induce as much shear stress as the continuous mode during photocuring when the part being printed is the most fragile and prone to failure; however, it requires more intricate control compared to the continuous mode (Section S1.2, Supporting Information). Using the CVP, the composite resin containing up to 30% w/w medium SrFe<sub>12</sub>O<sub>19</sub> particles (3–6 μm) is printable in the periodic mode. In contrast, the printing fails if the composite resin contains more than 0.1% w/w Fe<sub>3</sub>O<sub>4</sub> particle (50–100 nm), 0.5% w/w of Fe<sub>3</sub>O<sub>4</sub> particles (2–4 μm), or 5% w/w NdFeB particles (nominal size of 5 μm) because of the strong interference of these particles with the 405 nm light source; this prevents the resin from curing (Section S1.3, Supporting Information).

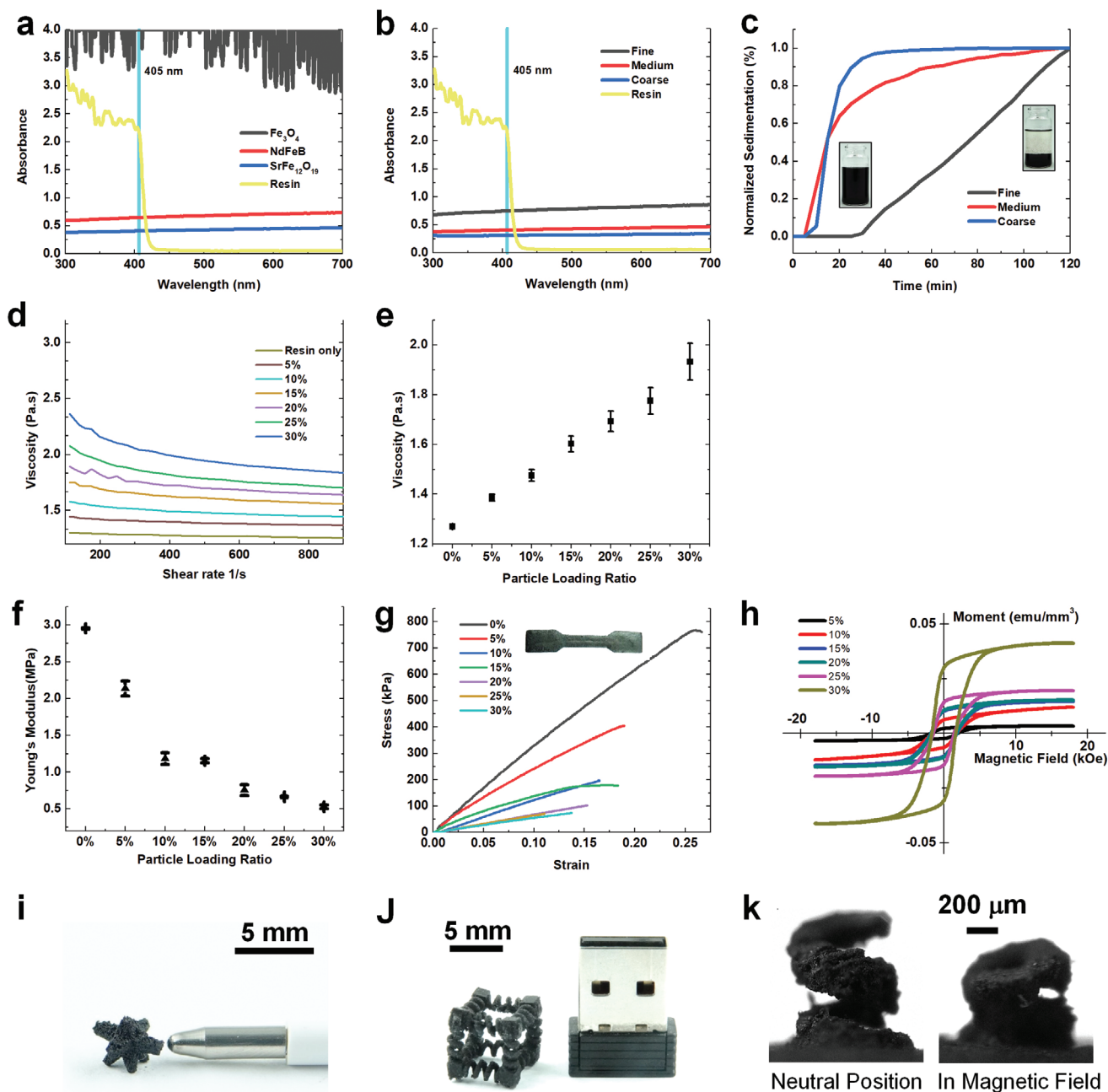


**Figure 2.** Characterization of CVP. a) Absorption spectra of  $\text{SrFe}_{12}\text{O}_{19}$ ,  $\text{NdFeB}$  and  $\text{Fe}_3\text{O}_4$  particles of similar size. b) Absorption spectrum of the  $\text{SrFe}_{12}\text{O}_{19}$  particles of different sizes. c) Sedimentation rate of  $\text{SrFe}_{12}\text{O}_{19}$  particles in the resin. d) Viscosity of composite resins containing various amounts of magnetic particles under different shear rates. e) Mean shear rate from 600 to 900  $\text{s}^{-1}$ . f) Tensile test of specimens printed by CVP with composite resins containing various amounts of magnetic particles. g) Young's modulus of these specimens. h) Magnetic hysteresis loop of parts printed by CVP with resins containing various amounts of magnetic particles. i–k) Various miniature magnetic 3D structures printed by CVP. k) The wire diameter and the external diameter of the magnetic spring are 300 and 900  $\mu\text{m}$ , respectively.

Consequently, a composite resin was formulated by blending medium  $\text{SrFe}_{12}\text{O}_{19}$  particles with a flexible PU-like resin to 3D print MSMR with CVP. The pure resin behaved as a Newtonian fluid with a viscosity of 1.27 Pa s as measured by frequency-sweep rheological testing. The composite resin started to exhibit shear-thinning behavior at low shear rates and reached a stable viscosity at higher shear rates with an increase in the loading of magnetic particles (Figure 2d). The mean viscosity

of the composite resin ( $600\text{--}900\text{ s}^{-1}$ ) increases with magnetic-particle-loading ratios (Figure 2e); however, it is generally low. The printed part became softer with an increase in the particle-loading ratios, as indicated by the decreasing Young's modulus in the tensile test (Figure 2f). This property is advantageous because both a high particle loading and a soft body are desirable features of MSMRs. The yield stress and fracture strain decrease simultaneously (Figure 2g), which indicates that parts

with higher particle-loading ratios break more easily upon stretching. The scanning electron microscopy (SEM) image of the specimen printed by CVP (Figure S1.5, Supporting Information) show that magnetic particles are trapped in the resin matrix; it is likely that magnetic particles are physically trapped instead of chemically bonded to the resin matrix. Physically trapped magnetic particles can disrupt the resin matrix and cause a loss in mechanical strength.

Magnetic responses of specimens printed by CVP are measured by vibrating-sample magnetometry (Figure 2h). The magnetic permeability and remanence of the specimens increased with an increase in the particle-loading ratios, which indicated that the printed part became more susceptible to the magnetic field and retained more residual magnetism after the external magnetic field was removed. However, the coercive force remained the same at all particle loading ratios, which implied that stronger external magnetic fields were not required to reverse the residual magnetism with an increase in the particle loading ratio. At their respective maximal loadings for CVP, SrFe<sub>12</sub>O<sub>19</sub> (30%) exhibited a more desirable magnetic response than NdFeB (5%) and Fe<sub>3</sub>O<sub>4</sub> (0.5%) (Figure S1.6, Supporting Information); it shows the highest magnetic saturation and remanence among the three, which suggests that parts printed with the SrFe<sub>12</sub>O<sub>19</sub> composite resin retain a high magnetism after magnetization (magnetically hard). Compared to Fe<sub>3</sub>O<sub>4</sub> and NdFeB, the large slope of SrFe<sub>12</sub>O<sub>19</sub> in the magnetic hysteresis loop indicates that it has a high permeability  $\mu_m$  and a high susceptibility  $\chi$  ( $\mu_m = \mu_r \mu_0$  and  $\chi = \mu_r - 1$ , where  $\mu_r$  and  $\mu_0$  represent the relative permeability and the permeability in free space). A high magnetic susceptibility  $\chi$  leads to a high magnetic torque  $\tau$  when exposed to an external magnetic field  $B_e$  according to  $\tau = \mathbf{m} \times \mathbf{B}_e$ , where  $\mathbf{m}$  represents the magnetic

moment  $\mathbf{m} = \chi \mathbf{H}$  and  $\mathbf{H}$  represents the true field in the magnetic material. Figure 2i–k shows several intricate true 3D structures printed by CVP with the SrFe<sub>12</sub>O<sub>19</sub> composite resin. The printing resolution with magnetic composite is similar to that attainable with the pure resin, which is limited by the resolution of the VP 3D printer (Figure S1.7, Supporting Information). The current work is demonstrated only on the XYZ Nobel 1.0A stereolithography 3D printer with a planar resolution of 130  $\mu\text{m}$  due to its openness for easy customization. The current CVP setup is able to create magnetically responsive spring with a wire diameter of 300  $\mu\text{m}$  and an external diameter of 900  $\mu\text{m}$  (Figure 2k), a range that is difficult for extrusion-based 3D printing to achieve. Furthermore, this concept can be applied to other types of VP 3D printers, such as microdigital light printing and two-photon photopolymerization, to achieve single-digit-micrometer or even sub-micrometer resolution.

### 3. MSMR Fabrication by CVP

Several tethered and untethered MSMRs were 3D printed using CVP. and their ability to manipulate droplets was demonstrated through magnetically controlled fully reversible shape morphing, which is a concept known as reversible 4D printing. In addition, we presented several biomimetic swimming MSMRs and showed their locomotion in a uniform magnetic field controlled by an electromagnetic coil system. The MSMRs have small and intricate 3D geometries that are difficult to fabricate using conventional methods.

An MSMR milligripper (Figure 3) is printed by CVP and rendered superhydrophobic by dip coating with 1% Teflon AF followed by the Ultra-Ever Dry top coat solution. The milligripper

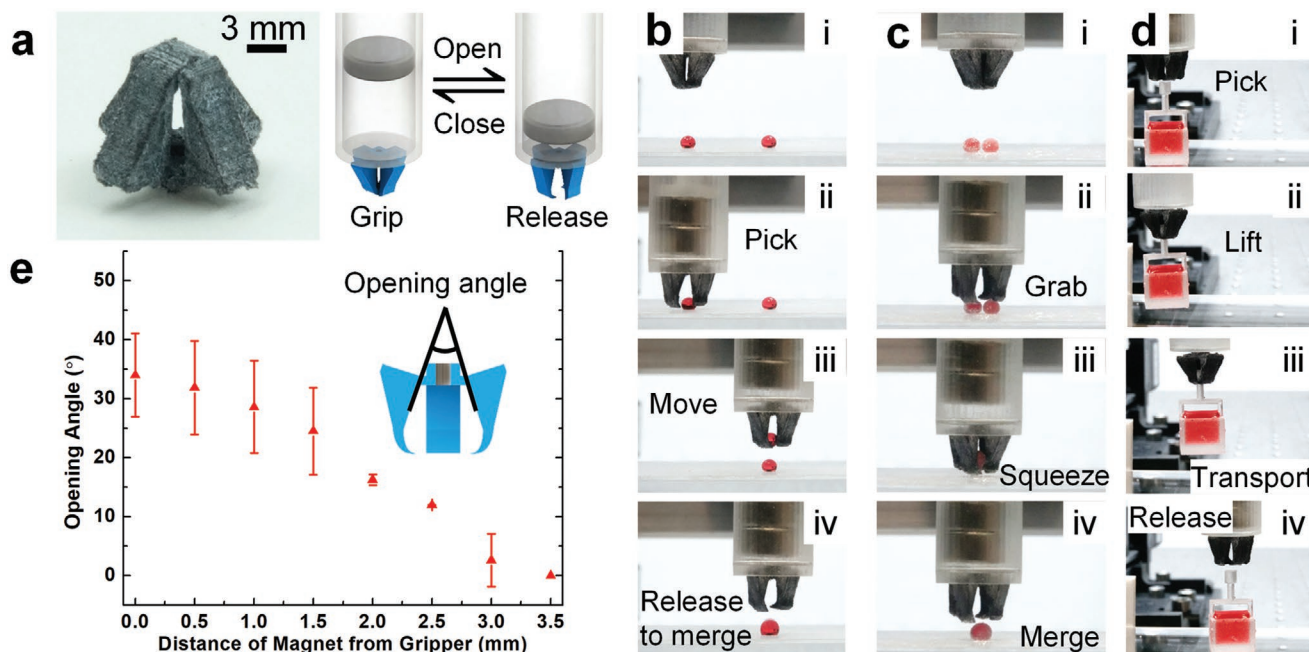


**Figure 3.** MSMR milligripper: a) design and working principle of the MSMR milligripper. b) Droplet manipulation with the MSMR milligripper. c) Liquid marble merging by squeezing with the MSMR milligripper. d) Lifting of solid objects by the MSMR milligripper. e) Opening angle of the milligripper versus the distance of the permanent magnet from its base.

consists of four finger joints connected to a base; the joints act as cantilevers that bend when exposed to an external magnetic field (Figure 3a). The base is attached to a control rod during the operation. The magnetic attraction force increases when the magnet in the control rod approaches the base of the milligripper, which causes the finger joints to bend and the milligripper to open. The elastic energy stored in the joints brings the milligripper back to its closed configuration once the magnet moves away. The milligripper can be programmed to pick up a water droplet on an open surface, move it to the location of the second droplet, and release it for droplet merging when mounted to a 3-axis translational stage (Figure 3b; Video S1\_1, Supporting Information). With the current design, the smallest droplet that can be picked up is 3  $\mu\text{L}$ , and the largest is 50  $\mu\text{L}$ . The MSMR milligripper offers unprecedented ease in manipulating tiny droplets in 3D. In addition to droplets, the MSMR milligripper can also manipulate liquid marbles. Liquid marbles are liquid droplets encapsulated by a layer of hydrophobic particles; they are difficult to merge because of this layer. Merging liquid marbles often requires accelerating them to a high speed<sup>[36]</sup> or applying an external electrical potential.<sup>[37]</sup> Merging by acceleration requires the liquid marbles to align in specific configurations that is hard to control, and the merged marbles often bounce in an uncontrolled manner. The electrical merging of liquid marbles requires a high voltage of hundreds to thousands of volts, and this poses a potential safety concern. Our MSMR milligripper offers a simple and controlled method of merging liquid marbles by squeezing them inside the gripper with only mechanical force, and it shows a 100% success rate (Figure 3c; Video S1\_2, Supporting Information). Although designed for the manipulation of liquid droplets, the MSMR milligripper is able to lift solid objects such as a 3D-printed mini bucket (Figure 3d; Video S1\_3, Supporting Information). By slowly adding water to the bucket, the maximum load that can be carried by the MSMR milligripper is determined to be 0.958 g. The milligripper (Figure 3e) opens up to 35° when fully open, and each finger generates a force of  $\approx 4.7$  mN at the maximal deflection. The MSMR milligripper becomes fully closed once the magnet is over 3.5 mm away from its base. The opening/closing speed reached 8.4° s<sup>-1</sup>, and no plastic deformation or fatigue was observed after 10000 reversible open-close cycles.

Furthermore, droplet manipulation was accomplished using two untethered MSMRs fabricated using CVP (Figure 4). The MSMR “caterpillar” comprises a head and a tail connected by two parallel springs (Figure 4a); the “rocking horse” comprises two legs connected by a horseback (Figure 4b). The key driving force of the locomotion for these millirobots are the magnetic force and spring force (Figure 4c). Two steps are performed to operate the “caterpillar.” In Step 1, a permanent magnet is positioned below the “caterpillar” and exerts a strong magnetic force  $F_T$  on the tail of the “caterpillar.” The horizontal component of  $F_T$  tends to pull the tail forward. As the tail moves forward, it compresses and stores elastic energy in the spring. Meanwhile, the magnet also exerts a strong vertical force on the head and thus a strong frictional force  $f_H$  that prevents the head from moving as the spring being compressed (Figure 4ci). The “caterpillar” reaches equilibrium when the spring is compressed to the maximum. In this case, the spring force that pushes tail is balanced by the frictional force on the tail  $f_T$  plus the horizontal component of the magnetic force  $F_T$  on the tail, and the spring

force that pushes head is balanced by the frictional force  $f_H$  on the head (Figure 4cii). In Step 2, the magnetic force decreases rapidly, and the spring force becomes the main driving force when the magnet moves away from the head. The compressed spring tends to push both the head and tail outward, but the frictional forces on both the head and tail resist the motion. Because the static friction force  $f_T$  on the tail is greater than that on the head due to larger contact area and heavier body of the tails, the head would be pushed forward by the spring force  $F_s$  while the tail is anchored by the frictional force  $f_T$  (Figure 4ciii). A stride is accomplished after these two steps are completed, and the spring is restored to its neutral position. This step-wise crawling of the MSMR “caterpillar” is utilized to magnetically control the movement of droplets on an open surface (Figure 4d; Video S2\_1, Supporting Information). As the head moves forward in each stride, it pushes the droplet to a designated location along a defined path. If the tail is fixed and the permanent magnet is quickly released, the MSMR “caterpillar” can accelerate the droplet like a pinball shooter, and this function empowers rapid droplet merging by shooting one droplet into another sessile droplet at a speed of 6.6 mm s<sup>-1</sup> (Figure 4e; Video S2\_2, Supporting Information; taken at 1000 fps). The MSMR “rocking horse” is operated in a way similar to the “caterpillar” except that the elastic energy is stored in the horseback instead of the spring (Figure 4f; Video S2\_3, Supporting Information). The “rocking horse” manages to kick two droplets with both of its legs (Figure 4fi). The two droplets are pushed forward one at a time in each stride. In Step 1, the magnet approaches the “rocking horse,” and the hind leg kicks Droplet 1 forward (Figure 4fii). In Step 2, as the magnet moves away, the foreleg kicks Droplet 2 forward (Figure 4fiii). The mean stride length for the “caterpillar” is about 2.86 mm or 20.4% of the body length, and the mean stride length for the “rocking horse” is about 2.81 mm or 28.1% of the body length (Figure 4g,h). The relative stride lengths of the “caterpillar” and “rocking horse” are comparable to molded MSMRs reported in earlier works whose stride length typical ranges from 15% to 29% of the body length.<sup>[11,16,38–40]</sup> A slight back stride of the tail/hind leg was observed in Step 2 of each stride; however, it did not affect the overall locomotion of these two millirobots.

Underwater millirobots hold great promise for minimally invasive surgery, precise drug delivery and other biomedical applications because they can maneuver through the aqueous environment in the human body.<sup>[17]</sup> An MSMR “jellyfish” comprising a hollow bell-shaped body with four flexible tentacles is designed as shown in Figure 4i. Despite its intricate 3D structure, the entire “jellyfish” is 3D printed monolithically and near-net-shape by CVP; hence, no postprinting assembly is required. The printed “jellyfish” is placed into a customized jig (Figure S2.1, Supporting Information) in a 1.1 T uniform magnetic field for the desired magnetization profile (Figure 4i). The “jellyfish” swam by flapping its tentacles up and down at a speed of 4.8 mm s<sup>-1</sup> at a frequency of 5 Hz (Figure 4j and Video S3\_1) when placed in an alternating magnetic field generated by a coil system consisting of nine electromagnets (Figure S2.2, Supporting Information). The tentacles flapped up when a magnetic field of 20 mT was applied (Figure 4jii). Further, the tentacles rapidly flapped down when a magnetic field of  $-8$  mT was applied (Figure 4jiii,jiv), and both the buoyancy of the hollow body and propelling force generated by the tentacles helped the

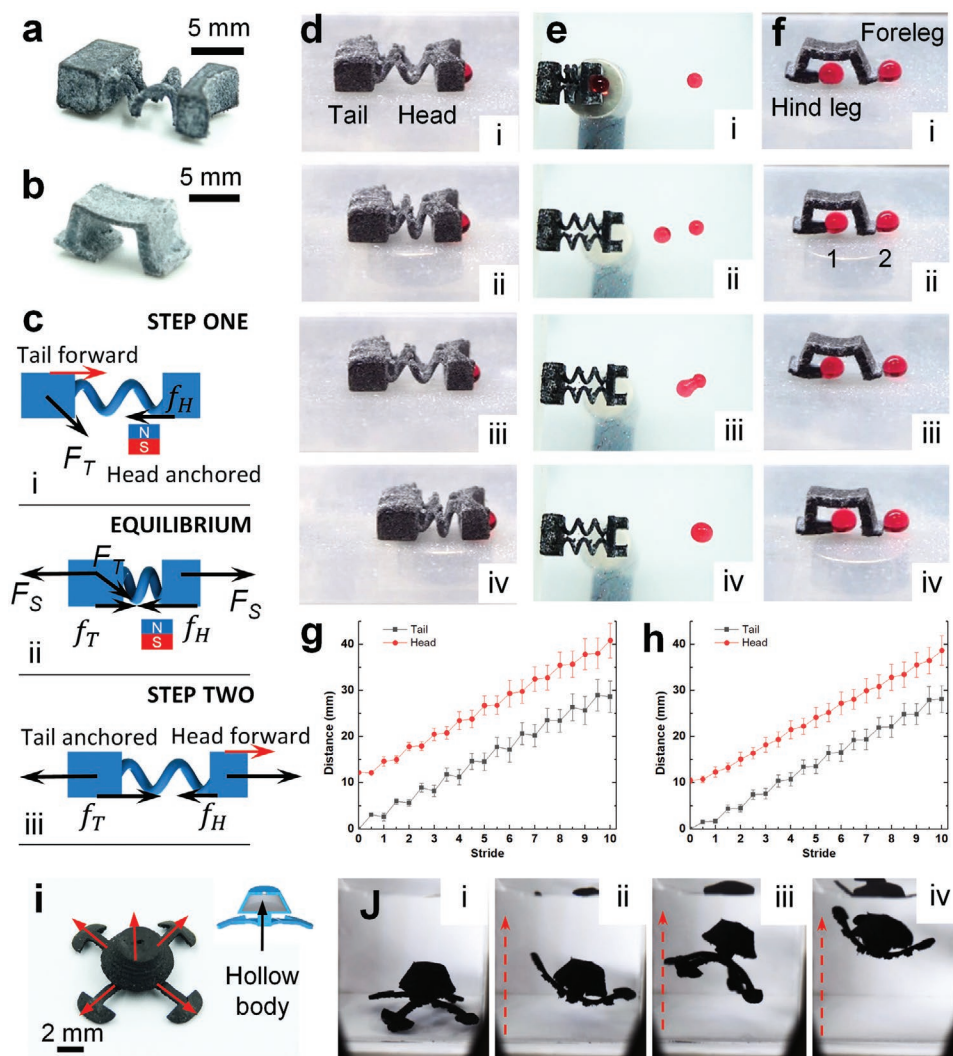


**Figure 4.** Untethered MSMR. a) MSMR caterpillar. b) MSMR rocking horse. c) Mechanism of caterpillar locomotion controlled by a permanent magnet. d) Droplet manipulation by the MSMR caterpillar. e) Shooting of droplets by the MSMR caterpillar. f) Droplet manipulation by the MSMR rocking horse. g) Stride length of the MSMR caterpillar. h) Stride length of the MSMR rocking horse. i) MSMR jellyfish and its magnetization profile. j) The MSMR jellyfish swims upward in an alternating magnetic field.

“jellyfish” to swim upward. Our proposed CVP method can also print rigid swimming millirobots. A magnetic “helicobacter” and a magnetic “fish” fabricated by CVP are demonstrated in Section S2.3 and Videos S3\_2–3\_4 (Supporting Information).

The MSMRs demonstrated above all require a high particle loading enabled by CVP for shape morphing in response to external magnetic fields. Regular VP typically prints magnetic composite with a loading at only around 0.5% w/w.<sup>[27]</sup> None of these MSMRs printed with such a loading ratio is able to morph their shapes in a strong magnetic field (Figure S2.4, Supporting Information).

#### 4. MSMR-Enabled Magnetic Microfluidic Handling Platform for Antimicrobial Resistance Detection

The ability of our MSMR to manipulate droplets makes them ideal for magnetic droplet manipulation. Magnetic droplet

manipulation is often performed on magnetic digital microfluidic platforms that conduct in vitro diagnostic assays in droplets controlled by magnetic particles<sup>[31,41–44]</sup> or magnetic substrates,<sup>[45]</sup> and they are capable of sample-to-answer molecular, immuno- and phenotypical assays<sup>[31]</sup> such as assays to detect drug resistance.<sup>[46,47]</sup> Carbapenemase-producing *Enterobacteriaceae* (CPE) is a group of Gram-negative drug-resistant bacteria classified as an urgent public threat—the highest level of threat.<sup>[48]</sup> The CPE bacteria are resistant to the antibiotic carbapenem, which is considered the last line of defense against bacterial infections.<sup>[49–52]</sup> As a proof of concept, we developed a fully automated MSMR-enabled magnetic digital microfluidic platform for CPE detection (Figure 5a). The platform comprises a toolbox, superhydrophobic reaction stage, and control rod to select and control the tools from the toolbox for reagent dispensing, sample addition, and droplet merging and mixing. The detailed structure and functions of these tools are provided in Section S3 (Supporting Information). The MSMR

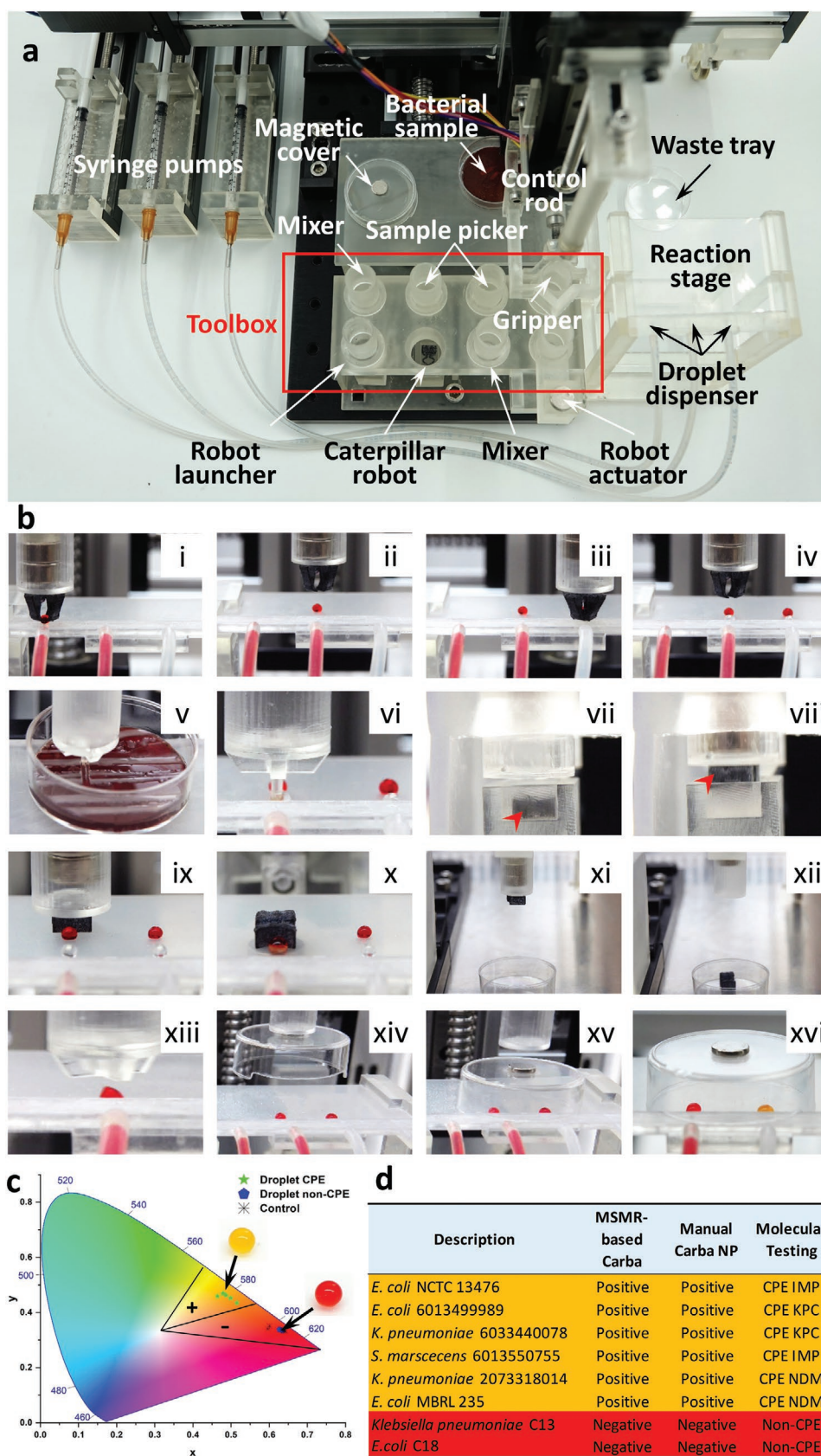


**Figure 5.** MSMR-empowered automated magnetic droplet microfluidic handling platform for in vitro diagnostics. a) Configuration of automated magnetic droplet microfluidic handling platform. b) Operation procedures to conduct Carba NP for the detection of CPE on the platform. i,ii) Dispense

milligripper first picked the reaction buffer droplet and sample buffer droplet (Figure 5bi–iv) from a microfluidic droplet dispenser (Figure S3.2, Supporting Information) and placed them on the reaction stage to conduct the Carba NP assay for CPE detection (Section S4 and Video S4\_1, Supporting Information). This is the first magnetic droplet microfluidic handling platform capable of dispensing a droplet of a specified volume and transferring it to any arbitrary location. The reaction buffer droplet (red droplet) on the right contained imipenem for testing, whereas the reaction buffer on the left did not contain imipenem and served as control. After all reagent droplets were dispensed and placed at the designated locations by the MSMR milligripper, the control rod selected the sample picker (nonmagnetic) to transfer the bacterial inoculum from the culture plate to both sample buffer droplets (clear droplet) (Figure 5bv). The tip of the sample picker was immersed in the sample buffer droplet for 2 min, during which the sample picker moved up and down every 30 seconds to resuspend the bacteria in the droplets (Figure 5bvi). Next, the MSMR “caterpillar” was deployed by the robot launcher to the reaction stage (Figure 5bvii–ix). The robot actuator then drove the “caterpillar” forward to merge the sample buffer droplet with the reaction buffer droplet (Figure 5bx). The first “caterpillar” was discarded into the waste tray by the robot actuator (Figure 5bxi–xii), and a second “caterpillar” was launched to complete the merging of the remaining two droplets. After merging, the mixer (nonmagnetic) stirred the droplets (Figure 5bxiii) for mixing, and both reaction droplets were covered with a petri dish and incubated at room temperature for 1 h (Figure 5bxiv–xvi). If the bacterial strain was CPE, it hydrolyzed imipenem, and the color of the reaction droplet turned from red to yellow. In contrast, the reaction droplet remained red when the bacterial strain was non-CPE. In both cases, the control reaction droplets (left) should remain red for the assay to be valid (Figure 5bxvi). The droplets were mapped to the CIE 1931 color space to objectively determine their colors (Figure 5c). A total of eight strains were tested on this platform, and the results agreed with the conventional Carba NP conducted in a microwell plate (Figure 5d; Figure S4.2, Supporting Information).

Our group previously developed a magnetic digital microfluidic platform to conduct Carba NP assay<sup>[46]</sup> in droplets for rapid CPE detection. On this platform, automated droplet manipulation was accomplished by magnetic particles; however, operations such as sample and reagent dispensing still require manual intervention. In the current work, MSMRs can perform 3D droplet transfer across different platforms, which enables fully automated droplet dispensing and manipulation; this reduces the risk of accidental exposure to hazardous biosamples and reagents when performing *in vitro* diagnostics.

## 5. Conclusion and Perspective

We present CVP, a new 3D printing technology to print MSMRs. The unique circulation system of CVP keeps magnetic composite resin homogenized, which allows the use of relatively large micrometer-sized particle fillers to print parts with high uniformity, high particle loading and strong magnetic response. We have optimized the magnetic composite resin, characterized the resin and printed parts, and demonstrated various functional MSMRs and their ability to manipulate droplets in 3D. Compared to many existing magnetic robots fabricated by molding or extrusion-based printing, MSMRs printed by CVP assume a true initial 3D geometry and can perform reversible 3D-to-3D transformation for locomotion and object manipulation. The maximum particle loading by CVP reaches 30%. Although this loading ratio is not as high as that used for molding, it is significantly higher than that typically used in regular VP which is around 0.5% w/w. Microrobots with 0.5% particle loading are usually rigid robots which are unable to perform 3D-to-3D transformation due to relatively weak magnetic force as shown in earlier works by other groups. In this study, we show that millirobots printed with 0.5% particle loading are unable to perform the desired tasks. MSMRs in earlier works are mainly used to manipulate solid objects, and most of them are done in a liquid environment to reduce the friction and exploit buoyant force to facilitate object manipulation. Our work, to our best knowledge, is the first that demonstrates liquid droplet manipulation by MSMRs and the first magnetic fluidic handling system that is capable of dispensing droplet of specified volumes and transfer the dispensed droplet to any arbitrary location.

As a proof of concept, we incorporated CVP-printed MSMRs into an *in vitro* diagnostic platform and demonstrated the automated detection of biohazardous antibiotic-resistant bacteria. This platform is a significant improvement on existing magnetic digital microfluidic systems that can only manipulate droplets on a plane surface and require manual droplet dispensing. Further, CVP significantly simplifies the fabrication of MSMRs and thus paves a new way for intricate 3D soft robots that are difficult to fabricate using conventional methods. Our proposed CVP method can be readily applied to the 3D printing of other composite materials, which is expected to lead to more functional parts with complex architecture and possibly new mechanisms for 4D printing. With CVP, we envision that more useful millirobots and microtools can be developed in the future to assist in both *in vitro* and *in vivo* biomedical applications.

Because the main objective of this study primarily focuses on the CVP-based 3D printing of MSMRs, the designs of MSMRs in this study are not optimized for best controllability

---

sample buffer droplet; iii,iv) dispense reaction buffer droplet; v) pick bacterial inoculum from the culture plate; vi) resuspend bacteria in the sample droplet; vii–ix) deploy the MSMR “caterpillar” onto the reaction stage; x) actuate “caterpillar” to merge the sample droplet with the reaction droplet; xi,xii) discard the MSMR “caterpillar”; xiii) mix liquids by stirring the droplet; xiv,xv) cover the droplets; xvi) incubate the reaction for 1 h. c) Carba NP test results mapped into CIE 1931 color space. All CPE strains stay in the “+” zone, and all non-CPE and control reactions stay in the “–” zone. d) Summary of Carba NP test results of eight bacterial strains. Results obtained on the MSMR-based magnetic digital microfluidic platform are benchmarked against conventional Carba NP and molecular testing.

and dexterity; they are designed to accomplish the required droplet manipulation tasks. This is the major limitation of this study. This concept of CVP can be applied to any vat polymerization platforms, such as two-photon photopolymerization, to 3D print objects with ultrahigh resolution. However, a stereolithography platform with a printing resolution of 130  $\mu\text{m}$  was selected for this study because of the openness of its hardware and firmware for customized modification. This relatively low resolution is another limitation of this study. We plan to implement CVP with microdigital light printing and two-photon photopolymerization to demonstrate the full capability of this technology, and design and 3D print microrobots with better controllability for more dexterous mobility based on high-resolution CVP in the future.

## 6. Experimental Section

**Magnetic Composite Resin:** The magnetic composite resin comprises a polyurethane-like resin (XYZ printing flexible resin B1) and magnetic particle fillers, including  $\text{Fe}_3\text{O}_4$  nanoparticles (50–100 nm, Sigma Aldrich),  $\text{Fe}_3\text{O}_4$  microparticles (2–4  $\mu\text{m}$ , ChemicalStore.com),  $\text{NdFeB}$  particles (nominal size 5  $\mu\text{m}$ , Magnequench), fine  $\text{SrFe}_{12}\text{O}_{19}$  particle (2.4–3  $\mu\text{m}$ , EASCHEM), medium  $\text{SrFe}_{12}\text{O}_{19}$  particle (3–6  $\mu\text{m}$ , Seatrend), or coarse  $\text{SrFe}_{12}\text{O}_{19}$  particle (6–12  $\mu\text{m}$ , Seatrend). The magnetic composite was homogenized for 5 minutes before use by an overhead stirrer operated at 1500 rpm.

**Surface Coating:** MSMRs were first dip-coated by immersing them in 1% Teflon AF (DuPont) solution for 5 min. Then, they were dried in an oven at 100  $^\circ\text{C}$  for 15 min before the second dip coating in the Ultra-Ever Dry top-coat solution (UltraTech) for 5 min. The coated MSMRs were dried again at 100  $^\circ\text{C}$  for 10 min before use; the resulting surface had a contact angle of  $\approx 170^\circ$ . The hydrophobic substrate was prepared by spin-coating a piece of acrylic sheet with 1% Teflon AF solution mixed with polytetrafluoroethylene powder at 3000 rpm for 1 min. The mixture was prepared by blending 2% w/w 1  $\mu\text{m}$  PTFE powder (Sigma Aldrich) with 1% Teflon AF solution and filtering the mixture with a 60-mesh sieve. The coated substrate was dried in an oven at 50  $^\circ\text{C}$  for 30 min before use; the resulting surface had a contact angle of  $\approx 165^\circ$ .

**Circulating Vat Photopolymerization (CVP):** The CVP prototype was built by modifying a stereolithography (SLA) 3D printing platform (XYZ Nobel 1.0A). A customized circulation system was integrated into the SLA platform to homogenize the composite resin during printing. A customized miniature resin vat with integrated inlets and outlets and a matching printing stage are used (Figure 1a), or a four-channel bifurcating fluidic manifold is attached to the original resin vat (Figure S1.1, Supporting Information). All customized parts were fabricated by 3D printing (Formlab 3 printer) with a rigid resin. More detailed information and operation of the CVP is available in Section S1 (Supporting Information).

**Absorbance of Magnetic Particles:** The absorbance of magnetic particles was measured with 0.2% w/w of magnetic particles suspended in glycerol. The UV–vis spectrometer (Biodrop) was blanked with glycerol, and the absorbance from 300 to 700 nm was measured by placing the composite resins in a cuvette with a 1 cm optical path.

**Particle Sedimentation Rate:** The sedimentation rates of three types of  $\text{SrFe}_{12}\text{O}_{19}$  particles were measured using a modified Westergren method. Composite resins containing 10% w/w  $\text{SrFe}_{12}\text{O}_{19}$  particles were fully homogenized before being filled into a cylindrical glass with a diameter of 27 mm. The levels of all three composite resins were maintained the same at 34 mm from the bottom of the glass vial. Sedimentation was recorded in a 2 h time lapse with a 5 min time interval. The height of the sediment layer (dark region at the bottom of the vial; Figure 2c, inset) was analyzed by using MATLAB and normalized between 0 and 1, where 1 was the height of the sediment layer at the end of 2 h.

**Viscosity Measurement:** The viscosities of the composite resins were determined by frequency-sweep rheological testing using a Rheometer (Discovery HR-2). 1 mL of the composite resin was added onto a 25.0 mm disposable parallel plate (ETC Aluminum). The shear rate was set from 0.001 to 1000  $\text{s}^{-1}$ , and the duration was set to 60 s. All the other parameters were maintained at the default values. Each sample was tested in triplicates at the room temperature (25  $^\circ\text{C}$ ).

**Tensile Test:** Standard tensile test coupons containing medium  $\text{SrFe}_{12}\text{O}_{19}$  particles at various particle-loading ratios were printed monolithically with composite resins. The dimensions of the coupons (Figure 2d) followed the ASTM D638 standard. The test was conducted using a tensile test machine (SHIMADZU) with a gauge length of 25 mm and a speed of 10  $\text{mm min}^{-1}$ . The stress–strain curves were plotted for each specimen. The value of Young's modulus was obtained from the slope of the stress–strain curve.

**Density Measurement:** The density of the specimens printed by CVP was measured using the Archimedes' method. Specimens ( $5 \times 5 \times 15 \text{ mm}^3$ ) printed with composite resins containing medium  $\text{SrFe}_{12}\text{O}_{19}$  particles at various particle-loading ratios were used. The measured density of the printed specimen  $\rho_s$  was given by  $\rho_s = m_s \rho_{\text{water}} / m_{\text{water}}$ , where  $m_s$ ,  $m_{\text{water}}$  and  $\rho_{\text{water}}$  represents the measured weight of the specimen, weight of the displaced water, and density of water, respectively.

**Vibrating-Sample Magnetometry (VSM):** The magnetic hysteresis loop was obtained by measuring a  $5 \times 5 \times 0.8 \text{ mm}^3$  specimen printed with composite resins containing medium  $\text{SrFe}_{12}\text{O}_{19}$  particles at various particle-loading ratios using VSM with a maximal field from –18 to 18 kOe, a field step size of 50 Oe, and an averaging time of 0.1 s. The specimen was attached to the sample holder using a sticker. The magnetic moments of each specimen were obtained under different magnetic fields. The magnetic moment density can be obtained by dividing the volume of each sample.

**Magnetic Soft Millirobots (MSMRs):** All MSMRs were 3D printed with a composite resin that containing 15% w/w  $\text{SrFe}_{12}\text{O}_{19}$  particles mixed in a flexible resin (XYZ printing resin B1) except for the caterpillar that used 10% w/w. It took 27, 18, 12, 13, 12, and 27 min to print the “milligripper,” “caterpillar,” “rocking horse,” “helicobacter,” “fish,” and “jellyfish,” respectively. The support structures were removed after printing. The printed parts were immersed in 99% ethanol for 10 min to remove the uncured resin. The hollow head chamber of the jellyfish was washed by rinsing the inner surface with a needle and syringe. After cleaning, the samples were dried for 5 min at room temperature before being placed in a UV chamber for 5 min for further curing. For all demonstrations with droplets shown in Figures 3 and 4, the volume of the droplet was 10  $\mu\text{L}$ . The water droplets were stained with red food dye to aid visualization. The permanent magnet used to control the magnetic millirobots had a magnetic strength of 250 mT (diameter, 10 mm; height, 5 mm). The two magnets were stacked and mounted to a motorized linear stage for automated motion control. The motion command was communicated through an Arduino microprocessor.

**Uniform Magnetic Field with Electromagnetic Coil System:** The electromagnetic coil system had a workspace of 16 mm  $\times$  16 mm  $\times$  16 mm which was surrounded by nine electromagnets with the configuration shown in Figure S2.2 (Supporting Information). Thus, uniform magnetic field in different directions can be obtained by controlling the currents in the coils according to the concept presented in the literature.<sup>[30,53]</sup> All the electromagnets can be simultaneously controlled using a customized UI in LabVIEW. The maximum magnetic field strength in the workspace was 20 mT in the XY direction and 30 mT in the Z direction.

**CPE Detection:** Bacterial strains were obtained from the National Center for Infectious Disease of Singapore, Mayo Clinic (Rochester, MN), as well as ATCC and NCTC. The identity of and comprised 6 CPE strains (2 IMP, 2 KPC and 2 NDM) and 2 non-CPE (Figure 5). All bacterial samples were stored in Microbank vials (Pro-Lab diagnostics) and kept at –80  $^\circ\text{C}$ . Before the experiment, all bacterial samples were subcultured twice and plated on 5% TSA sheep blood agar plates (Thermo Fisher Scientific) at 37  $^\circ\text{C}$  in ambient air overnight. The conventional Carba NP assay was conducted in microwell plate using a modified protocol

described by Vasoo et al.<sup>[54]</sup> The sample buffer contained 0.85% w/w physiological saline solution. Two types of reaction buffer were prepared. The first reaction buffer for the control reaction contained  $10 \times 10^{-3}$  M ZnSO<sub>4</sub> (Sigma Aldrich) and 0.5% (w/v) phenol red (Sigma Aldrich), and was titrated to pH 7.8 with 0.1 N NaOH. The second buffer for the testing reaction had the same composition as the first one with additional 6 mg mL<sup>-1</sup> imipenem (or 12 mg mL<sup>-1</sup> imipenem/Cilastatin Kabi). The Carba NP assay on the magnetic digital microfluidic platform was conducted using a modified described by Kanithamniyom et al.<sup>[46]</sup> All droplets in the assay were 10 μL in volume, a 90% reduction in reaction consumption compared to the conventional Carba NP assay in microwell plate. The assay principle and procedure are described in detail in Section S4 (Supporting Information).

## Supporting Information

Supporting Information is available from the Wiley Online Library or from the author.

## Acknowledgements

Y.Z. would like to thank the Singapore National Additive Manufacturing Innovation Cluster (NAMIC 2020034) and NTUive Gap funding (NGF-2020-08-002) for funding support. The authors would like to acknowledge NTU FACTS (Facility for Analysis, Characterization, Testing and Simulation) for providing the SEM service and training. The authors would also like to thank Dr. Alan Lim Ming Pin for his help with SEM and data analysis and Dr. Robin Patel for kindly sharing bacterial isolate MBRL 235 used in this study.

## Conflict of Interest

Y.Z. declares equity interest in Guangzhou DropLab Scientific Co. Ltd. and DropLab Scientific (Singapore) Pvt. Ltd.. The rest authors declare no conflict of interest.

## Author Contributions

Y.Z. conceptualized and supervised the project; Y.Z. and A.Z. developed the CVP, made the design, and planned the experiments; Y.Z., A.Z., G.Z.L., and X.Z. analyzed the data; A.Z., C.X., C.S.X.N. and G.Z.L. conducted the experiments on underwater millirobots; A.Z., P.K., and S.V. conducted experiments for CPE detection; A.Z., G.L., and W.S.L. conducted VSM experiments; A.Z. conducted the rest experiments; S.V. provided the bacteria strains; Y.Z., A.Z., X.Z., and G.Z.L. wrote, edited, and proved the manuscript.

## Data Availability Statement

The data that support the findings of this study are available from the corresponding author upon reasonable request.

## Keywords

3D printing, additive manufacturing, digital microfluidics, magnetic robots, millirobots

Received: January 4, 2022

Revised: February 1, 2022

Published online:

- [1] C. Hu, S. Pané, B. J. Nelson, *Annu. Rev. Control Robot. Auton. Syst.* **2018**, *1*, 53.
- [2] K.-J. Cho, J.-S. Koh, S. Kim, W.-S. Chu, Y. Hong, S.-H. Ahn, *Int. J. Precis. Eng. Manuf.* **2009**, *10*, 171.
- [3] S. Nocentini, C. Parmeggiani, D. Martella, D. S. Wiersma, *Adv. Opt. Mater.* **2018**, *6*, 1800207.
- [4] J. Z. Gul, M. Sajid, M. M. Rehman, G. U. Siddiqui, I. Shah, K. H. Kim, J. W. Lee, K. H. Choi, *Sci. Technol. Adv. Mater.* **2018**, *19*, 243.
- [5] J. Walker, T. Zidek, C. Harbel, S. Yoon, F. S. Strickland, S. Kumar, M. Shin, *Actuators* **2020**, *9*, 3.
- [6] T. J. Wallin, J. Pikul, R. F. Shepherd, *Nat. Rev. Mater.* **2018**, *3*, 84.
- [7] G. Dogangil, B. L. Davies, F. Rodriguez y Baena, *Proc. Inst. Mech. Eng. H* **2010**, *224*, 653.
- [8] D. Jang, J. Jeong, H. Song, S. K. Chung, *J. Micromech. Microeng.* **2019**, *29*, 053002.
- [9] M. Cianchetti, C. Laschi, A. Menciassi, P. Dario, *Nat. Rev. Mater.* **2018**, *3*, 143.
- [10] H. Ceylan, J. Giltinan, K. Kozielski, M. Sitti, *Lab Chip* **2017**, *17*, 1705.
- [11] W. Hu, G. Z. Lum, M. Mastrangeli, M. Sitti, *Nature* **2018**, *554*, 81.
- [12] H. J. Chung, A. M. Parsons, L. Zheng, *Adv. Intell. Syst.* **2020**, *3*, 2000186.
- [13] M. Sitti, D. S. Wiersma, *Adv. Mater.* **2020**, *32*, 1906766.
- [14] T. Xu, J. Zhang, M. Salehizadeh, O. Onaizah, E. Diller, *Sci. Rob.* **2019**, *4*, eaav4494.
- [15] X. Wang, G. Mao, J. Ge, M. Drack, G. S. Cañón Bermúdez, D. Wirthl, R. Illing, T. Kosub, L. Bischoff, C. Wang, J. Fassbender, M. Kaltenbrunner, D. Makarov, *Commun. Mater.* **2020**, *1*, 67.
- [16] J. Kim, S. E. Chung, S. E. Choi, H. Lee, J. Kim, S. Kwon, *Nat. Mater.* **2011**, *10*, 747.
- [17] G. Z. Lum, Z. Ye, X. Dong, H. Marvi, O. Erin, W. Hu, M. Sitti, *Proc. Natl. Acad. Sci. USA* **2016**, *113*, E6007.
- [18] I. Blanco, *J. Compos.* **2020**, *4*, 42.
- [19] H. Lee, Y. Jang, J. K. Choe, S. Lee, H. Song, J. P. Lee, N. Lone, J. Kim, *Sci. Rob.* **2020**, *5*, eaay9024.
- [20] N. W. Bartlett, M. T. Tolley, J. T. B. Overvelde, J. C. Weaver, B. Mosadegh, K. Bertoldi, G. M. Whitesides, R. J. Wood, *Science* **2015**, *349*, 161.
- [21] J. D. Carrico, T. Hermans, K. J. Kim, K. K. Leang, *Sci. Rep.* **2019**, *9*, 17482.
- [22] J. D. Hubbard, R. Acevedo, K. M. Edwards, A. T. Alsharhan, Z. Wen, J. Landry, K. Wang, S. Schaffer, R. D. Sochol, *Sci. Adv.* **2021**, *7*, eabe5257.
- [23] Y. Kim, H. Yuk, R. Zhao, S. A. Chester, X. Zhao, *Nature* **2018**, *558*, 274.
- [24] E. Sacyani Keneth, A. Kamyshny, M. Totaro, L. Beccai, S. Magdassi, *Adv. Mater.* **2021**, *33*, 2003387.
- [25] S. Tian, H. Zhao, N. Lewinski, *Bioprinting* **2021**, *23*, e00156.
- [26] U. Bozuyuk, O. Yasa, I. C. Yasa, H. Ceylan, S. Kizilel, M. Sitti, *ACS Nano* **2018**, *12*, 9617.
- [27] H. Ceylan, I. C. Yasa, O. Yasa, A. F. Tabak, J. Giltinan, M. Sitti, *ACS Nano* **2019**, *13*, 3353.
- [28] I. C. Yasa, H. Ceylan, U. Bozuyuk, A.-M. Wild, M. Sitti, *Sci. Rob.* **2020**, *5*, eaaz3867.
- [29] Ceylan, H., N. O. Dogan, I. C. Yasa, M. N. Musaoglu, Z. U. Kulali, M. Sitti, *Sci. Adv.* **2021**, *7*, eabh0273.
- [30] C. Xu, Z. Yang, G. Z. Lum, *Adv. Mater.* **2021**, *33*, 2100170.
- [31] Y. Zhang, N. T. Nguyen, *Lab Chip* **2017**, *17*, 994.
- [32] N. Löwa, J.-M. Fabert, D. Gutkelch, H. Paysen, O. Kosch, F. Wiekhorst, *J. Magn. Magn. Mater.* **2019**, *469*, 456.
- [33] I. C. Yasa, H. Ceylan, U. Bozuyuk, A.-M. Wild, M. Sitti, *Sci. Rob.* **2020**, *5*, eaaz3867.
- [34] W. W. Wits, S. Carmignato, F. Zanini, T. H. J. Vaneker, *CIRP Ann. Manuf. Technol.* **2016**, *65*, 201.
- [35] I. Niskanen, V. Forsberg, D. Zakrisson, S. Reza, M. Hummelgård, B. Andres, I. Fedorov, T. Suopajärvi, H. Liimatainen, G. Thungström, *Chem. Eng. Sci.* **2019**, *201*, 222.

- [36] J. Jin, C. H. Ooi, D. V. Dao, N. T. Nguyen, *Soft Matter* **2018**, *14*, 4160.
- [37] Z. Liu, X. Fu, B. P. Binks, H. C. Shum, *Soft Matter* **2017**, *13*, 119.
- [38] S. Wu, C. M. Hamel, Q. Ze, F. Yang, H. J. Qi, R. Zhao, *Adv. Intell. Syst.* **2020**, *2*, 2000060.
- [39] X. Yang, W. Shang, H. Lu, Y. Liu, L. Yang, R. Tan, X. Wu, Y. Shen, *Sci. Rob.* **2020**, *5*, eabc8191.
- [40] Y. Ju, R. Hu, Y. Xie, J. Yao, X. Li, Y. Lv, X. Han, Q. Cao, L. Li, *Nano Energy* **2021**, *87*, 106169.
- [41] P. Kanitthamniyom, A. Zhou, S. Feng, A. Liu, S. Vasoo, Y. Zhang, *Microsyst. Nanoeng.* **2020**, *6*, 48.
- [42] Y. Zhang, *Curr. Med. Chem.* **2021**, *28*, 6323.
- [43] P. Kanitthamniyom, Y. Zhang, *Electrophoresis* **2019**, *40*, 1178.
- [44] Y. Zhang, T. H. Wang, *Adv. Mater.* **2013**, *25*, 2903.
- [45] P. Irajizad, S. Ray, N. Farokhnia, M. Hasnain, S. Baldelli, H. Ghasemi, *Adv. Mater. Interfaces* **2017**, *4*, 1700009.
- [46] P. Kanitthamniyom, P. Y. Hon, A. Zhou, M. Y. Abdad, Z. Y. Leow, N. B. M. Yazid, V. L. W. Xun, S. Vasoo, Y. Zhang, *Microsyst. Nanoeng.* **2021**, *7*, 47.
- [47] Y. Zhang, D. J. Shin, T. H. Wang, *Lab Chip* **2013**, *13*, 4827.
- [48] T. Khawcharoenporn, S. Vasoo, K. Singh, *Emerg. Med. Int.* **2013**, *2013*, 258517.
- [49] Y. Doi, D. L. Paterson, *Semin. Respir. Crit. Care Med.* **2015**, *36*, 74.
- [50] E. Tacconelli, N. Magrini, G. Kahlmeter, N. Singh, Global Priority List of Antibiotic-Resistant Bacteria to Guide Research, Discovery, and Development of New Antibiotics, World Health Organization, 2017, [https://www.who.int/medicines/publications/WHO-PPL-Short\\_Summary\\_25Feb-ET\\_NM\\_WHO.pdf](https://www.who.int/medicines/publications/WHO-PPL-Short_Summary_25Feb-ET_NM_WHO.pdf), **2017**, *27*, 318.
- [51] M. J. Schwaber, Y. Carmeli, *JAMA, J. Am. Med. Assoc.* **2008**, *300*, 2911.
- [52] C.-C. Sheu, Y.-T. Chang, S.-Y. Lin, Y.-H. Chen, P.-R. Hsueh, *Front. Microbiol.* **2019**, *10*, 80.
- [53] M. P. Kummer, J. J. Abbott, B. E. Kratochvil, R. Borer, A. Sengul, B. J. Nelson, *IEEE Trans. Rob.* **2010**, *26*, 1006.
- [54] S. Vasoo, S. A. Cunningham, P. C. Kohner, P. J. Simner, J. N. Mandrekar, K. Lolans, M. K. Hayden, R. Patel, *J. Clin. Microbiol.* **2013**, *51*, 3097.